A98-31536

ICAS-98-3,2,1

FLOW PHYSICS OF LEADING-EDGE VORTEX-BREAKDOWN

X. Z. Huang and E.S. Hanff

Institute for Aerospace Research, National Research Council of Canada
Ottawa, Ont. Canada, K1A 0R6, Tel (613) 990-6796, Fax (613) 952-7677

Abstract

The behaviors of leading edge vortex and its breakdown, such as vortex core position, the movement of breakdown location, fluctuation, bifurcation and different time scale in the breakdown region as well as surface topology evolution, have been presented. These studies are prerequisites for proper modeling the aerodynamics when vortex breakdown is involved.

Introduction

High-performance aircraft must be capable of flying at high incidence and high angular rates, conditions under which airloads exhibit severe non-linearities and time dependence that cannot be modeled by conventional locally linearized techniques. The Non-Linear Indicial Response (NIR) method proposed by Tobak et al. provides a rational framework for solving flight dynamics problems in the presence of these effects[1]. However, prior to applying the NIR or any other modeling method, the complex flow under advanced maneuvering conditions must be reasonably well understood in order to obtain usable results.

Thus the Institute for Aerospace Research (IAR) and Wright Laboratory (WL, recently renamed AFRL) undertook a joint program in the late 1980's to explore the aerodynamics associated with advanced maneuvers[2]. Extensive wind-tunnel tests on configurations with a 65° delta wing at high incidence were conducted at IAR's 2 m x 3 m wind tunnel and at WL's 7 ft x 10 ft SARL facility[3] as well as in the IAR water tunnel[4] Most of the wind-tunnel experiments were performed at M=0.3 and Re_C=2.4x10^6. Static, forced oscillatory rolling, free-to-roll as well as ramp/hold pitching experiments were conducted to obtain force/moment and unsteady surface pressures data and surface as well as off-surface flow visualization. In addition, complementary water-tunnel flow visualization experiments were performed on a series of delta wings with sweep angles ranging from 55° to 75°. The extensive experimental data clearly demonstrated the complex behavior of leading-edge vortex breakdown and its dominant role in determining the aforementioned airload non-linearities and time dependence. This paper focuses on some of the flow visualization results in order to set foundation for further modeling of the aerodynamics.

Flow visualization experimental set-up

Fig. 1 shows the geometry of 65° delta wing model used in the wind tunnel. The model could be installed either on the roll or pitch rig. The former is capable of rolling the model in the forced or free-to-roll mode around its body axis. The maximum amplitude for harmonic oscillation is 40° about an offset of up to ±50° at frequencies up to 18 Hz [3]. The pitch rig pitches the delta wing model around an axis 22% of center chord behind the trailing edge. The maximum angle of attack range is from 0° to 90° with a minimum transition time between these values of 75 ms [5].

The leading-edge vortex was visualized by seeding the flow with smoke (in the static and rolling experiments) and applying a laser light sheet normal to the body axis, whereas in the pitching experiments natural condensation was used to provide the needed seeding and the light sheet was oriented longitudinally passing through the vortex core over most of its length. In order to optimize flow visualization in the smoke tests, the plume was adjusted to impinge just aft of the model apex. The smoke particles originally contained within the boundary layer on the model lower surface were entrained, upon separation at the sharp leading edge, into the shear layer which then rolled into the primary vortices, resulting in very little smoke being present elsewhere on the lee of the model. In order to obtain a reasonably high temporal resolution, images were captured by a high-speed video camera with a frame rate of up to 1000 fps. Video frames were individually analyzed to determine the vortex geometry on the basis of the local image intensity.

In general, a cross-sectional view of an intact vortex appears as a ring of high brightness with a dark core, whereas a burst vortex appears as an evenly illuminated disk with somewhat more diffuse edges. The breakdown location determined using this criterion tends to be aft of the actual location of the kink of the vortex, as it is difficult to identify the kink from this type of view. Occasionally, particularly near the apex, the darker sub-core is not discernible due to saturation of the video camera. The edge of the vortex core was assumed to be where the maximum intensity gradient occurs. Once the edge was defined, the core diameter and position relative to the model were determined as well as the radial intensity profile.

Complementary flow visualization experiments were conducted on a family of delta wings with and without centerbody as well as different sweepback angles, thickness, and leading- and trailing-edge angles. A freestream velocity U_∞ = 5.3 in/sec corresponding to a Reynolds number of 36,000/ft was used. Maximum model length and span were limited to 5 in to avoid excessive blockage. Dye was injected through two 0.008 in. diameter ports located at 5% of c_0 and half of local semi-span on the windward side. Two video cameras provide a top and side view of the vortices. Breakdown was defined at the kink of the vortex filament.

Surface flow topology was obtained in the static tests by applying a mixture of mineral and/or silicone oils and titanium dioxide to the model. The viscosity of the mixture was tailored to optimize the observation of the desired features. Photographs were taken to capture the

surface flow patterns during and after the run High-resolution videos recorded the development of those patterns and were used to resolve some ambiguities in the flow direction near the surface. Flow patterns were recorded at a wide range of roll angles at selected sting angles so that a large number of topologies would be identified. Particular attention was placed on the evolution of the flow topology as a function of the roll angle, particularly in regions where static load discontinuities were observed

General description of leading-edge vortex

Flow separating at the sharp leading-edge of a delta wing at moderate to high incidence forms a free shear layer that eventually rolls up into fully developed leading-edge vortices that feature a viscous core, with the vortex flow around it being essentially inviscid. When the vorticity-feeding rate from the leading edge exceeds that that can be convected downstream, the vortex filaments tighten up leading to breakdown. The unsteady mixing in the breakdown zone dissipates vorticity and causes a turbulent wake as well as loss of lift.

The chordwise distribution of gray level profiles of the leading edge vortices for the 65° delta wing for a sting angle σ=30° and different roll angles are shown in Fig. 2. In all cases the intact vortices are curved inboard. This curvature is probably due to the presence of the center body and the leading-edge bevel, both of which have more effect on the flow in the front part of the model due to their relative larger size compared with the local semi-span.

The normal and spanwise locations of the vortex center under static and dynamic conditions are shown in Fig. 3, where it can be seen that he normal position, z/s, is approximately 0.3 regardless of the chordwise station, roll angle and roll rate. The spanwise location does vary as a function of roll angle but is independent to roll rate. Fig. 4 shows the non-dimensional rotational vortex diameter D/s over the left wing as a function of x for different roll angles, where s is the local semi-span. Breakdown occurs approximately for D/s = 0.5.

Fluctuation and bifurcation of vortex breakdown

Large-scale fluctuations in the breakdown location have been observed even under static conditions. Fig. 5 shows two typical longitudinal sections of the leading edge vortex obtained at the same attitude, highlighting the unsteadiness in the breakdown region even in the low turbulence SARL facility, equipped with a 36:1 contraction ratio. To facilitate descriptions, the vortex filament kink associated with the onset of breakdown is denoted as point A in Fig. 5 while the subsequent turbulent breakdown is denoted as point B. Interestingly, the locations of point B are nearly the same in both cases, whereas the locations of point A are quite different. The dark circles in Fig. 5a correspond to cross-sections of the spiral vortex core, which are not visible in Fig. 5b due to the lower azimuthal vorticity associated with the lower spiral divergence.

To illustrate the high level of unsteadiness in the breakdown process, selected pairs of consecutive frames are shown in Fig. 6 where the frame number is included. Frames in the first and second pairs are separated by 4 ms while the frames in the last pair are taken 1 ms apart, corresponding to 0.60 and 0.15 convection times, c/U_∞, respectively. These typical figures show that the length of the spiral breakdown region can change significantly within a convection time indicating that the propagation speed of point A can approach $0.5U_\infty\cos\alpha$ whereas the very small displacement of point B reflects a much lower propagation speed. Furthermore, Fig. 6 suggests that for a given angle of attack when the instantaneous flow conditions promotes vortex breakdown, point A moves rapidly forward while point B hardly moves, resulting in an increase of the helix angle, a reduction in the spiral diameter with the pitch remaining more or less constant. On the other hand when the instantaneous flow condition delays breakdown, point A moves rapidly downstream with point B again responding very slowly, resulting in a decrease of the helix angle and an increase in the spiral diameter, with pitch again remaining more or less constant. The length of the breakdown region therefore changes mainly as a result of changes in the number of spiral turns contained therein. The additional loops needed to lengthen the breakdown region seem to be generated by a curling up of the previously intact vortex just forward of point A. Likewise a straightening of the upstream turns within the breakdown region seems to cause its shortening

Significantly larger fluctuations of the breakdown location were observed when breakdown occurred over the leading- and trailing-edge bevels as demonstrated by the standard and maximum deviations plotted in Fig.7. This result was obtained in a water tunnel for 65° delta wing with 10° leading- and trailing edge bevels. It appears that the increased fluctuations near the leading- and trailing-edge bevels are due to the presence of geometric discontinuities.

In order to assess the stability of the breakdown process, water-tunnel experiments were conducted in which an obstruction was introduced aft of the breakdown point. In most cases this resulted in the expected forward displacement of the corresponding breakdown point [6] which quickly returned to its original position once the obstruction was removed. The other breakdown point moved in the opposite direction. In some cases involving the 75° flat delta wing, however, unexpected results were obtained when breakdown occurred near the trailing edge. For example at an angle-of-attack of 32° breakdown initially occurred symmetrically at $x_{VB}\approx0.9$, and the temporary introduction of a small obstruction caused an effect analogous to the above. However if the obstruction was introduced closer to the breakdown point, its effect was larger, causing it to move even further than before. Upon removal of the obstruction the breakdown point quickly moved back to a stable position approximately 5% upstream of the initial symmetric point. In the meantime the breakdown point on the other wing half commenced a gradual motion that would place it well aft of the trailing edge, taking over hundred freestream convection times to reach a stable position at $x_{VB}\approx1.4$. Application of the

disturbance aft of the latter could either lead to a reversal of the situation or a symmetric arrangement. The various breakdown responses and eventual locations were repeatable, suggesting that more than one stable solution exists. The attractor basin associated with the symmetric arrangement was much smaller than that for the asymmetric ones. An example of the motion history of the two breakdown points as a result of the application and removal of a disturbance is shown in Fig. 8, where long waiting times have been removed for the sake of clarity.

Geometry effect on breakdown location

A great deal of work has been conducted by a number of investigators to establish the effect of leading edge geometry and the presence of a centerbody on vortex behavior on delta wings[6,7,9]. Here we focus on some new findings and clarifying some unclear points.

The time-averaged vortex-breakdown location observed in the water tunnel for flat wings with sweep angles ranging from 55° to 75° are shown in Fig. 9. The results. particularly for the slenderer wings exhibit a more gradual movement over the trailing edge than those reported by Wentz[7] agreeing with those of Lawson[9] and Delery[6]. Furthermore, the breakdown point over the trailing edge of the 70° delta wing proved to remain quite stable confirming that the so-called knee phenomena, characterized by a rapid, almost jump-wise movement of the breakdown location from mid-chord to the trailing edge[7,8] are atypical[9] and cannot be confused with possible discontinuities associated with the presence of a leeside trailing edge bevel.

Fig. 10a shows the breakdown locations over 65° delta wings observed by various investigators. It can be seen that the IAR/WL results obtained at higher Re than the others is delayed by a approximately 20% root chord, raising the issue of a possible effect of the leading and trailing edge bevels. This was investigated in the water tunnel using 65° deltas of the same size but different thickness, all with 10° bevels, resulting in wider bevels on the thicker wings. The corresponding results are presented in Fig. 10b which shows that the thinner the wing the closer breakdown occurs to that on a flat one. Breakdown is delayed about 5~6% for the intermediate thickness model, while that for the thickest one approaches the locations observed in the IAR/WL wind-tunnel experiments. The latter correspond approximately to predictions based on an effective angle corrected by the kinematic expression, $\Delta\alpha=\delta_L \cos\Psi$. The above results suggest that the effectiveness of the leading-edge bevel in delaying breakdown appears to be related to the ratio between leading-edge width and pre-separation boundary layer thickness. In fact this ratio is 15 times larger in the wind-tunnel experiments than that for the thickest model in the water tunnel ones. It is clear that in the case of the thin model the pressure gradient is largely dictated by the flat leeward surface. Water-tunnel experiments confirmed that the presence of a trailing edge bevel mainly delays breakdown in the aft part of the wing as shown in Fig. 11 while a centerbody has a small delaying effect (Fig. 12a and 12b), largely in agreement with Pelletier's results[10]

Motion effects on breakdown location

Under dynamic conditions, the behavior of the leading-edge vortex is considerably more complex, largely because of the above mentioned slow breakdown response. As an illustration, the gray level profiles at different instantaneous roll angles for the case of an oscillation amplitude of $\Delta\phi=40°$, k=0.04 and $\sigma=30°$ are shown in Fig. 13. The vortex spanwise location, local diameter and breakdown location can be observed through the complete oscillation cycle by following the appropriate sequence of images. These have been arranged in pairs of opposite angular rates at given roll angles in order to highlight the dramatic motion effects, which can also be appreciated by comparing these results with the static results in Fig. 2. At $\phi=0°$ under oscillatory conditions the vortex only exists over one wing half depending on the rolling direction as opposed to the symmetry prevailing statically. Furthermore, for $\phi=4°$ and to a lesser extent for $\phi=8°$ the vortices on the two wing halves are reasonably symmetric for opposite roll rates, again indicating the dominance of dynamic effects.

Fig. 14 shows the non-dimensional vortex diameter vs. roll angle over the right wing half at several stations for different oscillation frequencies. The static results, based on the average value over the intact vortex are also included for comparison. Each dynamic trajectory has two branches, the left and right ones corresponding to the upstroke and downstroke respectively. The first point on the left branch and the last one on the right branch correspond to the formation and breakdown of the vortex at the indicated stations. For a given roll angle, the dynamic D/s is larger than the corresponding static value during the upstroke, while it is smaller during the downstroke. The difference between the dynamic and static values increases with amplitude and frequency, although at higher angular rates this process tends to saturate.

There is overwhelming evidence that the motion of leading-edge vortex breakdown plays an important role in creating the non-linearities and time dependence of airloads observed under dynamic conditions[11,12]. Considerable effort has, therefore, been directed at observing the response of breakdown to model motions. The determination of the breakdown location is, however, hindered under dynamic conditions by a relative paucity of video frames which renders more difficult the averaging process. Considerable judgment must be exercised in determining the breakdown location, which unavoidably introduces some inaccuracy.

The effect of oscillation frequency on breakdown motion over the right wing half is shown in Fig. 15. The dramatically lagged response to the rolling oscillation results in a loop even at very low reduced frequencies and becomes more pronounced at higher frequencies. The differences between the results at k=0.14 and k=0.2 are relatively small due to the saturation process alluded to above. The longitudinal range traversed by the breakdown point decreases at higher frequencies due to its limited propagation speed, which has been found to be

approximately 0.1 U_∞ and 0.2 U_∞ in the forward and aft directions respectively. Sections of the loops near the apex and trailing edge are not shown due to insufficient frames to reliably establish the breakdown location. The effect of amplitude is shown in Fig. 16. In this case the loops tend to expand rather evenly with amplitude without exhibiting saturation, suggesting a more linear effect than that of frequency.

Likewise, under transient pitching conditions, significant time lags in the breakdown point location are present. Model motion also causes axial compression and expansion of the breakdown region between points A and B, both effects being a function of motion history. As an illustration, the ensemble-averaged position of point A and B for the case of pitch-down transition from α=30° to 20° are depicted in Fig. 17a where the static ones are superimposed for comparison. The corresponding phase plane diagram of the model motion is shown in Fig. 17b. Initially, breakdown is at its static location and moves aft when the angle of attack decreases. However, in spite of the small reduced angular rate, the instantaneous breakdown location rapidly falls behind its static counterpart. Furthermore, the distance between point A and point B tends to be smaller than under static conditions as the former tries to "catch up with the latter".

Effect of a pitch-up motion between α=20° and 50° at different angular rates are shown in Fig. 18a and Fig. 18b. In both cases breakdown is aft of the trailing edge at the motion onset and moves on to the wing at an angle of attack which depends on the angular rate. Interestingly, at the lower rate the instantaneous breakdown location tends to approach its static value (Fig. 18a), while the angular rate is still increasing. At the higher angular rate breakdown reaches the trailing edge much later (α=31) with a considerably larger distance between points A and B.

Fluctuations in the breakdown location associated with flow unsteadiness are also observed under dynamic conditions. Fig. 19 shows two consecutive images taken 1 ms apart at instantaneous angles of attack α=24.43° and α=24.40° during a pitch down maneuver α=50° to 0°. Instead of moving downstream due to the motion, point A exhibits a clear upstream displacement, whereas point B remains approximately fixed. This behavior is consistent with the above-mentioned difference in response times of the two points.

Flow topology structures

The presence of leading-edge vortex breakdown causes a number of flow field structural changes as a function of a state variable, in this case roll angle, which are reflected in various skin friction line topologies. An important step in understanding the flow physics is to recognize the existence of these flow structures and associated behavior. As the roll angle changes, the original streamline solution may become unstable, leading to a bifurcation that results in different solutions that, in turn, may be stable or unstable to small perturbations. Specifically, the bifurcation can lead to either a new time invariant equilibrium state, a stable periodic oscillation (Hopf bifurcation) or even multiple time invariant and/or non-time invariant equilibrium states (Liapunov bifurcation).

An understanding of the topological changes due to parameter variation may shed some light onto the complicated nature of three-dimensional flow separation and critical states in airloads. Thus, surface flow visualization tests were conducted at σ=30° and 35° for a large range of roll angles to obtain the evolution of the surface flow topology in terms of roll angle. Those topology patterns could be classified into five major patterns: concentrated vortex, P1, (Fig. 20 and 21); vortex "whorl", P2, (Fig. 22); bursting vortex, P3, (Fig. 23); reverse flow, P4, (Fig. 24) and totally separated flow (P5). The sequence represents the patterns in the order in which they would appear on the port wing half as the model is rolled from 62° to.-62° Each pattern may include sub-patterns depending on the roll angle. A summary of the topological patterns is shown on Fig. 25 for different roll and sting angles.

The concentrated vortex pattern (P1) shown in Fig. 20 occurs in the presence of fully intact primary and secondary vortices. It generally appears on the leeward wing half at very large roll angles. This pattern is present on the port wing half in Fig. 25(a) to Fig. 25(d) where the primary separation line is at the leading-edge and the primary reattachment line is shown by N_{a2} - S_4. The secondary separation and the reattachment lines are S_2 - N_{s2} and N_{a3} - S_3 respectively. Under these conditions the tertiary separation and reattachment lines could not be observed, probably due to a combination of insufficient primary vortex strength and insufficient boundary layer mixing length due to the outboard primary vortex location (Fig. 21). There is disagreement regarding the location of the tertiary vortex. In Ref. 6 it is assumed to be outboard of the secondary vortex as shown in the cross section view in Fig. 26a while in Ref. 13 it is located inboard of the secondary vortex (Fig. 26b). The surface topology is the same and the only difference is in a reversal of reattachment lines A2 and A3. The present authors believe that the latter is a better interpretation of the actual flow field.

At lower roll angles a "whorl" pattern (P2) develops on the leeward wing half, characterized by the presence of at least one "whorl" corresponding to a spiral node, N_F, occurring when a vortex sharply lifts off from the surface. Initially a single "whorl" appears due to the tertiary vortex lifting off the surface (Fig. 22a and $P2_1$ in Fig. 25e). As the roll angle is decreased further, the whorl moves forward and a second whorl reflecting the lift-off of the secondary vortex appears as well (Fig. 22b and $P2_2$ in Fig. 25f). Further reduction in the roll angle results in the disappearance of, first the tertiary (Fig. 22c and $P2_3$ in Fig. 25g) and then the secondary, whorl.

Further reductions in the roll angle result in the primary vortex breakdown moving on to the leeward wing half, leading to a bursting vortex pattern (P3). Fig. 23a shows oil flow patterns for σ = 30° and ϕ=0° and Fig. 23b to Fig. 23d for σ = 35° and ϕ=2.5°. The corresponding surface flow topologies are shown by

patterns $P3_1$ and $P3_2$ in Fig. 25f and Fig. 25h respectively. The breakdown is indicated by a kink on the secondary separation line which topologically requires a higher-order singular point consisting of a separation node and a saddle ($(N_S S)_1$). In $P3_1$ the separation and reattachment of the tertiary vortex can be readily observed. Moreover the tertiary vortex separation line merges into the corresponding secondary one. In $P3_2$ on the other hand, the tertiary lines are not discernible. Since the tertiary vortex can only exist upstream of the primary vortex breakdown, it is not clear whether in this case the tertiary vortex does not exist or it only exists near the apex of the model where there is insufficient resolution to observe it. If the latter is true, $P3_2$ would not be a legitimate pattern.

Once the wing half under consideration is sufficiently to windward, and breakdown is near or at the apex, a variety of reverse flow patterns may develop as shown in Fig. 24a to Fig. 24e. Similar patterns could occur at large sideslip angles and lower angles of attack if spiral flow is present, although, in this case, the primary vortex may not exist due to insufficient vorticity feeding rate. The corresponding topologies $P4_1$ to $P4_4$, are depicted for the right wing half in Fig. 25a to Fig. 25e and Fig. 25g to Fig. 25h. In all these patterns there is an interaction of a leading-edge separation induced spiral flow and a reverse flow, which leads to one or more stable separation foci. As the wing half rolls further to windward, the reverse flow increases due to the trailing edge acting increasingly like a side edge, which in turn forces the axis of the spiral flow to lift off the surface creating the above foci.

, At extreme roll angles, the spiral flow over the windward half disappears suddenly leaving a separation bubble. Under these conditions no discernible oil pattern is produced (P5) leading to its exclusion from Fig.25.

Fig. 27 shows possible three-dimensional flow field interpretations leading to some of the previously described surface flow topologies. Flow patterns on the model for a variety of attitudes are listed in Table 1. In some cases there is an uncertainly regarding a particular pattern due to limitations in the image quality or due to excessive flow unsteadiness that does not seem to result in a discernible mean pattern. It is important to note that the above topological analysis, being based on oil patterns, reflects a time average of the skin friction lines which is representative of the actual flow only under time invariant equilibrium states. Furthermore, there is no unique correspondence between a given skin friction line topology and the 3D flow field. In order to resolve possible ambiguities it is necessary to have additional information such as surface pressure gradient[14].

Topological changes vis-à-vis critical states

Knowledge of the topological evolution is also useful to identify critical states, defined as points within the motion history where Frèchet differentiability of the aerodynamic response functionals is lost[1]. An important step for understanding and applying the NIR method is the recognition of the existence and effects of these critical states. A listing of the experimentally determined critical states for the 65° delta wing[15,16].is shown in the table below together with topological changes observed at approximately the same roll angles.

Cr. states	Tp. changes	Main observations
σ=29°,ϕ=5°	$P3_1$:$P3_1 \leftrightarrow P2_2$:$P3_1$	two whorls appear
σ=29°,ϕ=8.2°	$P2_2$:$P3_1 \leftrightarrow P2_2$:$P4_1$	secondary vortex disappears a very weak focus appears
σ=29°,ϕ=11.6°	$P2_2$:$P4_1 \leftrightarrow P2_2$:$P4_1$	a whorl disappears
σ=29°,ϕ=50.1°	$P1_1$:$P4_2 \leftrightarrow P1_1$:$P4_4$	a focus splits into two foci
σ=29°,ϕ=51.5°	$P1_1$:$P4_4 \leftrightarrow P1_1$:$P_s$	skin-friction line disappears
σ=35°,ϕ=1.2°	$P3_1$:$P3_1 \leftrightarrow P3_1$:$P3_2$	secondary vortex disappears
σ=35°,ϕ=3.5°	$P3_1$:$P3_2 \leftrightarrow P3_1$:$P4_1$	secondary vortex disappears a very weak focus appears
σ=35°,ϕ=62.1°	$P1_1$:$P4_3 \leftrightarrow P1_1$:$P4_5$	a large focus appears

In addition to the listed, some topology changes, for example, $P2_1$:$P4_1 \leftrightarrow P1_1$:$P4_1$ and $P1_1$:$P4_1 \leftrightarrow P1_1$:$P4_2$ for σ=30°, ϕ=14°~16° and σ=35°, ϕ=21° are not associated with a measurable critical state. When topology changes from $P2_1$ to $P1_1$, the only change is in the tertiary vortex. In the change from $P4_1$ to $P4_2$ the original focus of separation near mid chord on the windward wing half splits up into three singularities that may have a minimal effect on the forces. It should be noted, however, that critical states are associated with bifurcation in the solution of the Navier-Stokes equation which do not necessarily correspond to bifurcation in the time-average surface topology. Understanding the possible links between topological changes and critical states is of considerable interest from a flight mechanics point of view and is the subject of on-going investigations.

Conclusions

- The normal position of the leading-edge vortex on a 65° delta wing is virtually independent of roll angle and rolling rate, while the spanwise position is a function of roll angle but not rate. Time lags in both cases are negligible.
- The vortex is weakened during the downstroke as demonstrated by a decreasing D/s and strengthened during the upstroke.
- Two time scales appear to apply in the breakdown region: the onset of breakdown (point A) has a fast (convective) time scale whereas the turbulent breakdown (point B) is associated with a much longer response time, which result in the breakdown region exhibiting non-linear compression and stretching characteristics.
- Under some conditions, when breakdown occurs near the trailing edge, more than one mean breakdown location may exist.
- No knee was found for the time-averaged vortex breakdown location over slender delta wings.
- The effectiveness of a leeward leading-edge bevel seems to depend on the ratio of bevel width to pre-separation boundary layer thickness.

- Breakdown motion exhibits very large delays under dynamic conditions.
- The presence of breakdown introduces a number of topology changes in terms of roll angle. Five main surface flow patterns and ten different sub-patterns have been identified depending on angle of attack and roll angle.

References

1. Tobak, M., Chapman, G.T., and Unal, A., "Modeling Aerodynamic Discontinuities and Onset of Chaos in Flight Dynamical System," NASA TM-89420, 1986.Nonlinear Problem in Flight
2. Jenkins, J. and Hanff, E.S., "Highlights of the IAR/WL Delta Wing Program," Workshop III: Delta Wings-Unsteady Aerodynamics and Modeling, AIAA Atmospheric Flight Mechanics Conference, August 1995.
3. Hanff, E.S. and Huang, X.Z., "Rolling and Pitching Experiments on Configurations with a 65° Delta Wing at High Incidence," NRC/IAR LTR-A-013, 1997.
4. Huang, X.Z., Sun, Y.Z. and Hanff, E.S., "Further Investigations of Leading-Edge Vortex Breakdown Over Delta Wings," AIAA Paper 97-2263, 1997.
5. Hanff, E.S. and Huang, X.Z., "Highlights of the IAR/WL High-Alpha Joint Program," NPU/AIAA AFM 96-016, 1996.
6. Delery, J.M., " Aspect of Vortex Breakdown," Prog. Aerospace Sci. Vol. 30, pp. 1-59, 1994.
7. Wentz, W.H. Jr. and Kohlman, D.L., "Vortex Breakdown on Slender Sharp-Edged Wings," AIAA Paper 69-778, 1969.
8. Ericsson, L.E., "Prediction of Vortex Breakdown Effects on a Rolling Delta Wing," AIAA Paper 94-1883, 1994.
9. Lowson, M.V. and Riley, A.J., "Vortex Breakdown Control by Delta Wing Geometry," AIAA Paper 94-3487.
10. Pelletier, A. "An Experimental Study of Static and Dynamic Vortex Breeakdown on Slender Delta Wing Planforms," AIAA Paper 94-1879, 1994
11. Huang, X.Z. and Hanff, E.S., "Prediction of Leading Edge Vortex Breakdown on a Delta Wing Oscillating in Roll," AIAA Paper 92-2677.
12. Huang, X.Z. and Hanff, E.S., "Prediction of Normal Force on a Delta Wing Rolling at High Incidence," AIAA Paper 93-3686.
13. Chaderjian, N.M., "Navier-Stokes Prediction of Large-Amplitude Delta-Wing Roll Oscillations," J. of Aircraft, Vol. 31, No. 6, pp. 1333-1340, 1994.
14. Dallmann, U., "On the Formation of Three-Dimensional Vortex Flow Structure," DFVLR-IB 221-85 A13, 1985.
15. Jenkins, J.E., Myatt and Hanff, E.S. "Body-Axis Rolling Motion Critical States of a 65° Delta Wing," AIAA Paper 93-0621, Jan., 1993
16. Jobe, C.E., Hsia, A.H., Jenkins, J.E., and Addington, G.A., "Critical States and Flow Structure on a 65° Delta Wing," J. of Aircraft, Vol. 33, No. 2, March-April, 1996.

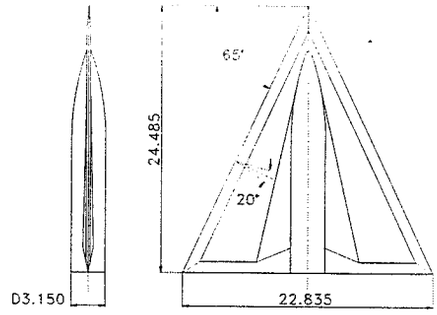

Fig. 1 65° delta wing model

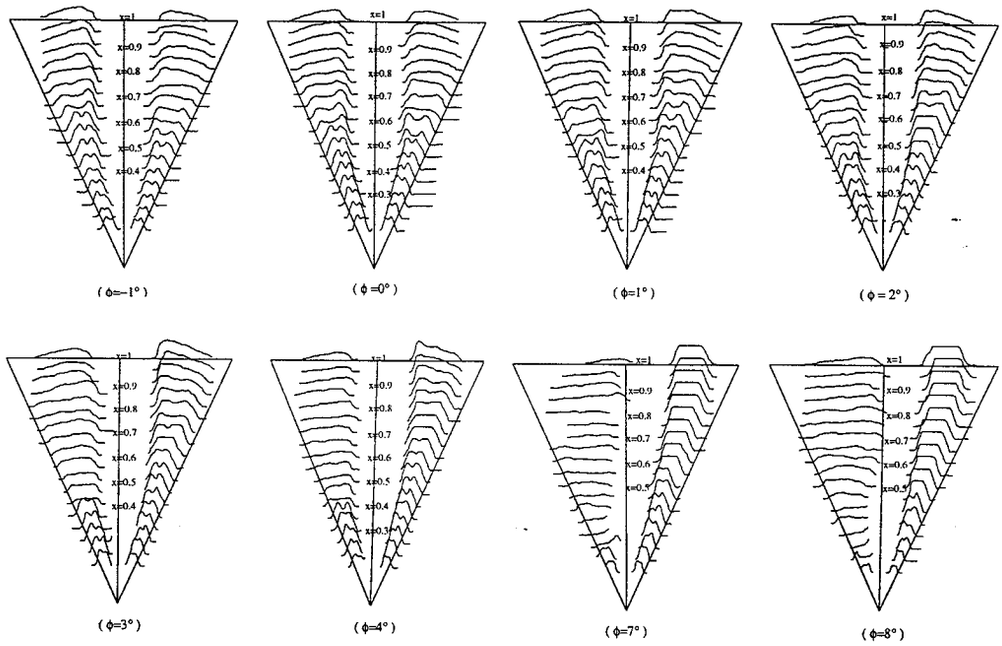

Fig. 2 Gray level profiles through vortex core at different stations (static, σ=30°)

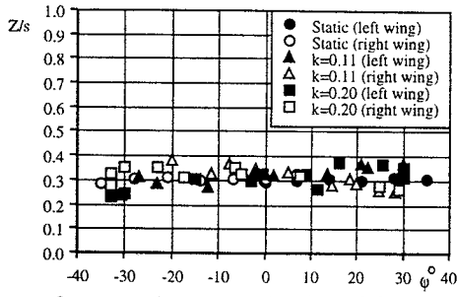

3a normal positions (static and dynamic)

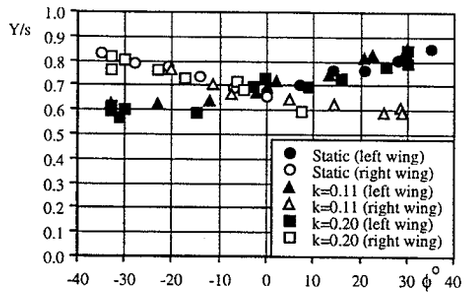

3b spanwise positions (static and dynamic)

Fig. 3 Measured vortex core positions (σ=30°)

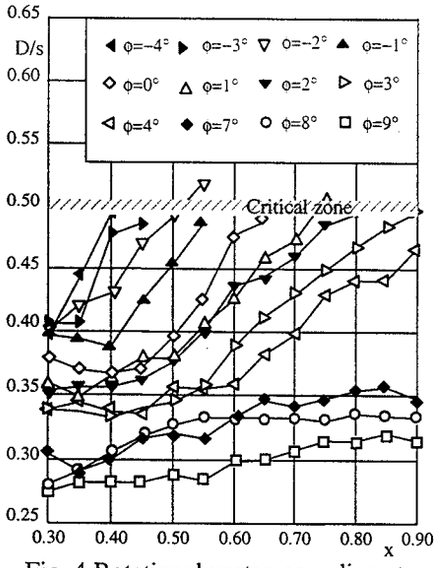

Fig. 4 Rotational vortex core diameter over left wing (σ=30°, static)

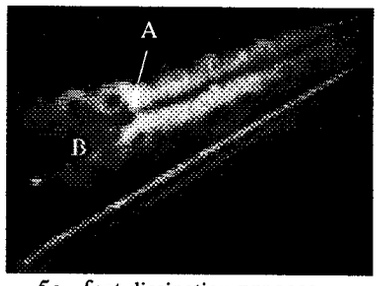

5a fast dissipation process

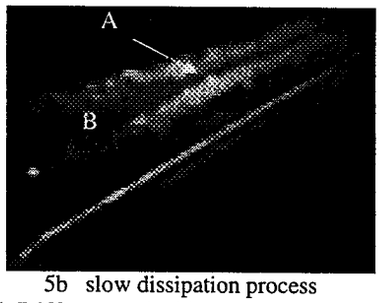

5b slow dissipation process

Fig. 5 Different spiral breakdown appearances (α=26°)

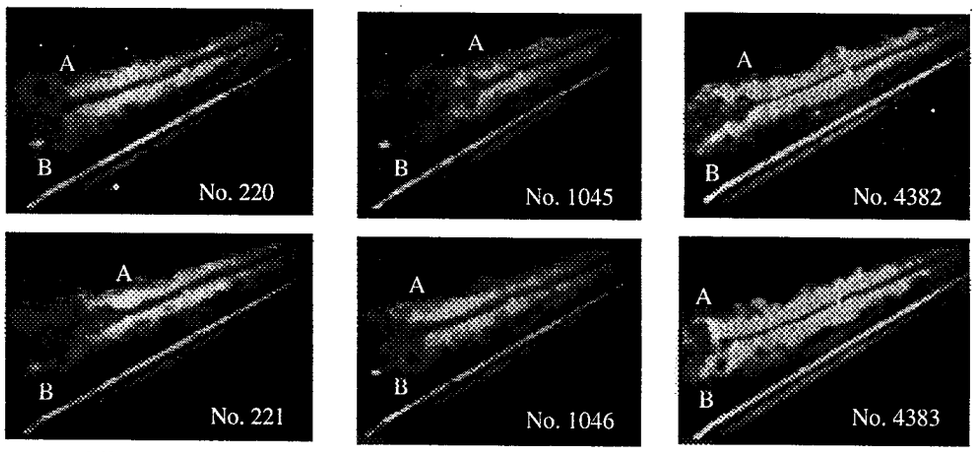

α=26°, Δt=4 ms (0.60τ) α=26°, Δt=4 ms (0.60τ) α=25.5°, Δt=1 ms (0.15τ)

Fig. 6 Pairs of vortex breakdown images

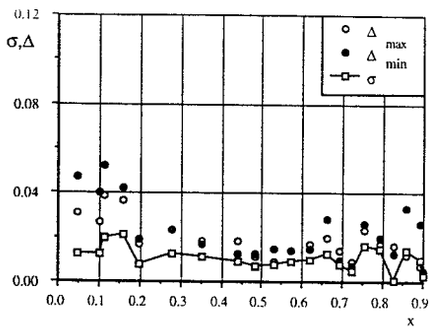

Fig. 7 Effect of bevel discontinuity on data scatter

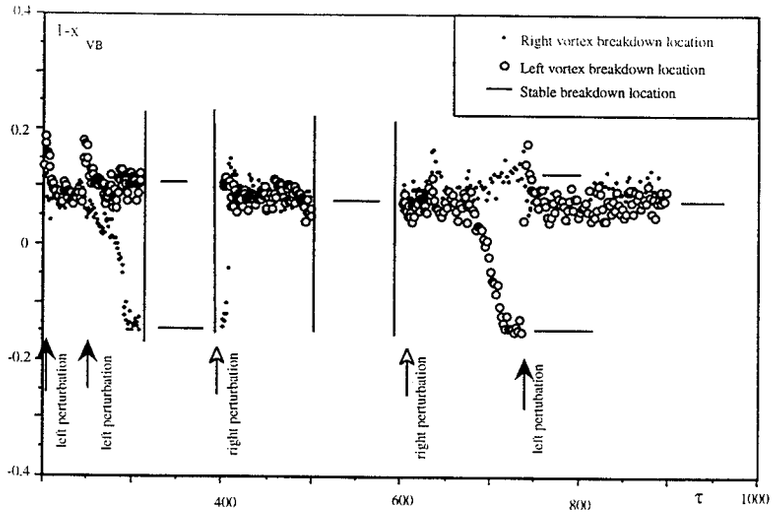

Fig. 8 Observed bifurcation of breakdown locations (Ψ=75°, α=32°)

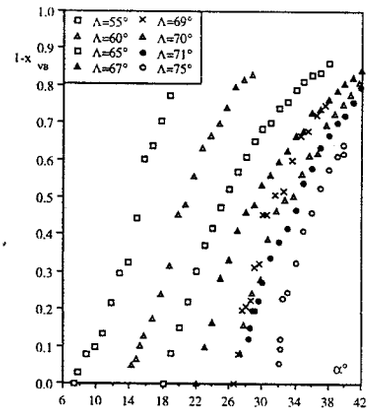

Fig. 9 Sweepback angle effect on breakdown locations

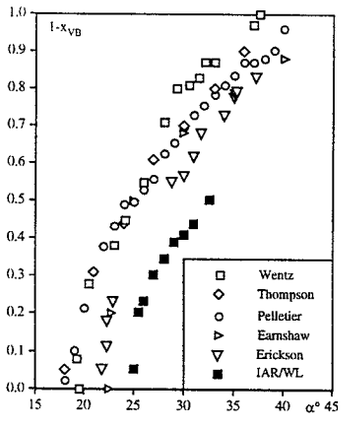

10a breakdown locations

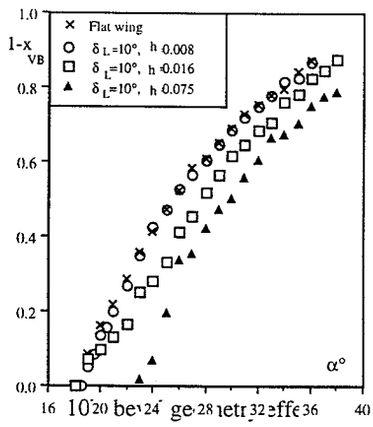

Fig. 10 Breakdown locations and leading-edge bevel effect (Ψ=65°)

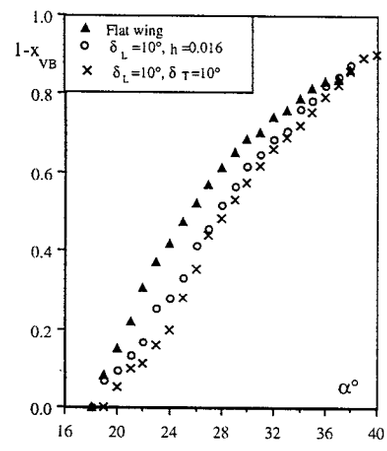

Fig. 11 Effect of leading-edge and trailing edge bevel (Ψ=65°)

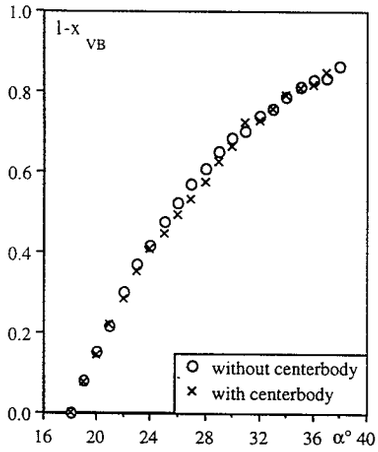

12a flat wing

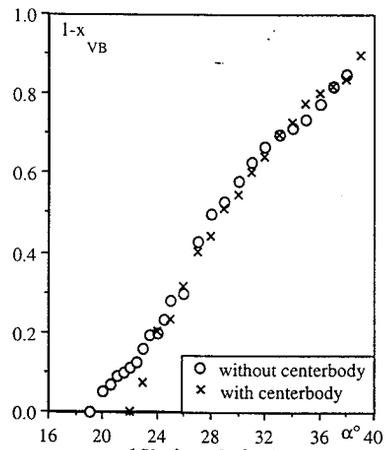

12b beveled wing
($\delta_L = \delta_T = 10°$)

Fig. 12 Center body effect on vortex breakdown location (Ψ=65°)

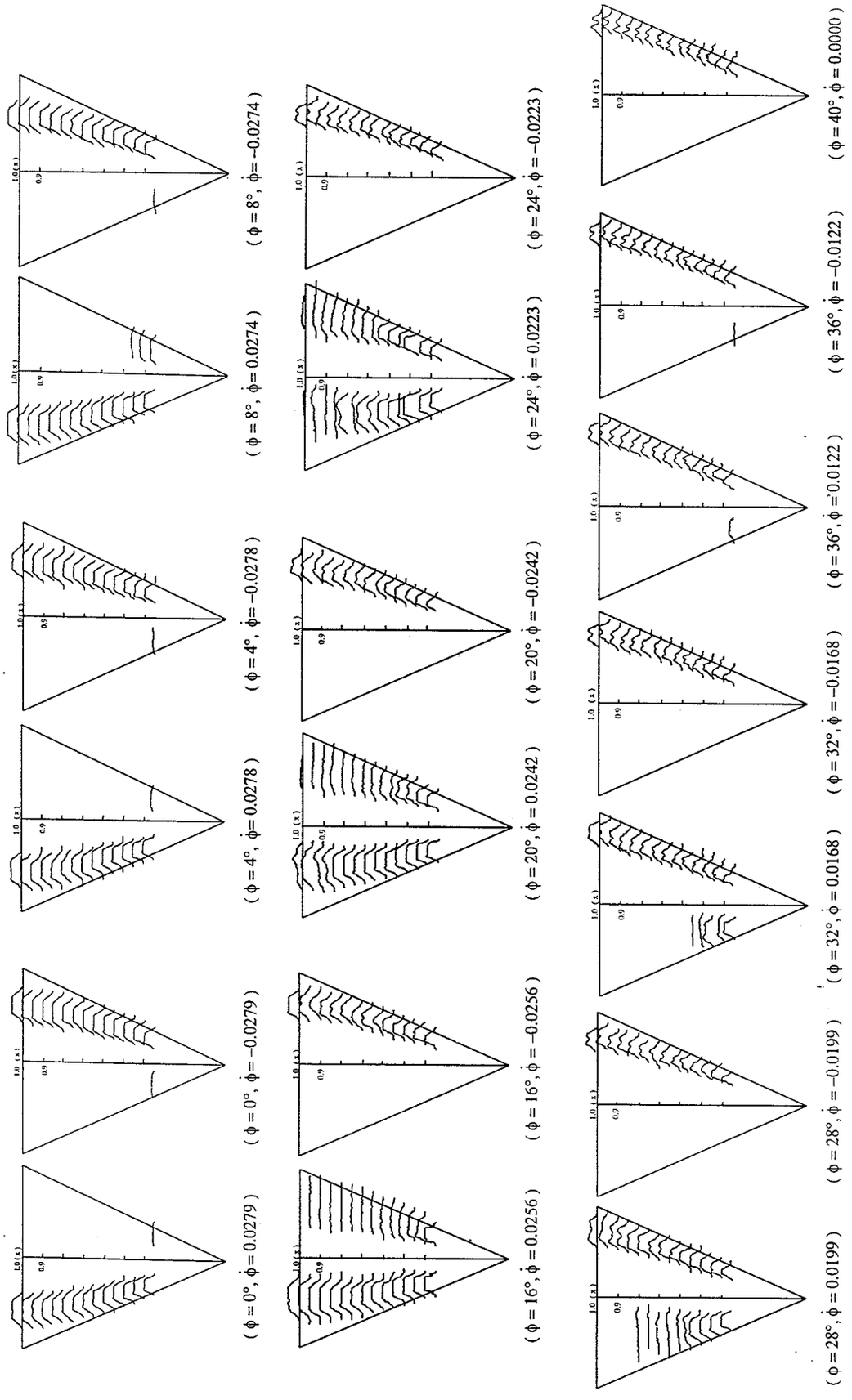

Fig. 13 Gray level profiles through vortex core under oscillatory conditions
($\sigma = 30°$, $\Delta\phi = 40°$, $k = 0.04$, $\phi_0 = 0°$)

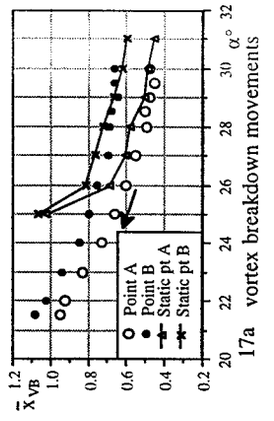

Fig. 17 Breakdown movement during pitch-down

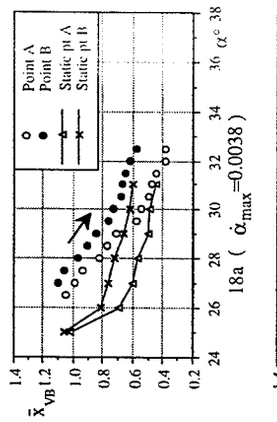

Fig. 18 Breakdown movement during pitch-up with different rates (α: 20°→50°)

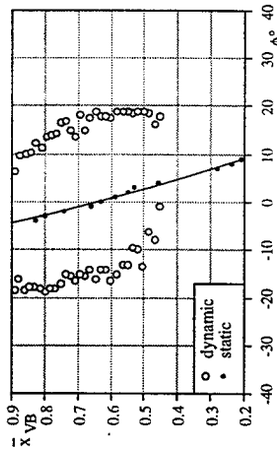

Fig. 16 Amplitude effect on vortex breakdown

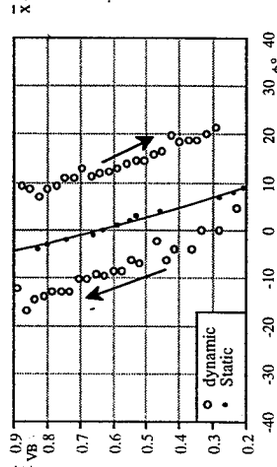

Fig. 15 Frequency effect on vortex breakdown

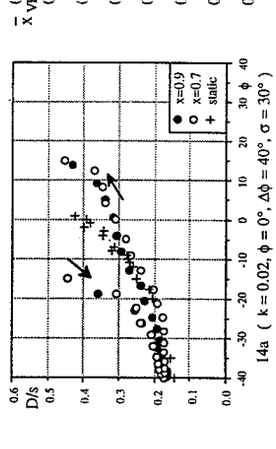

Fig. 14 Rotational vortex core diameter under oscillatory conditions

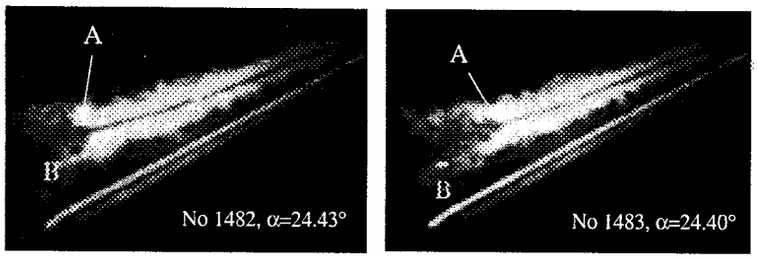

Fig. 19 Breakdown fluctuation during pitch-down motion
(α: 50° → 0°. Δt =1ms)

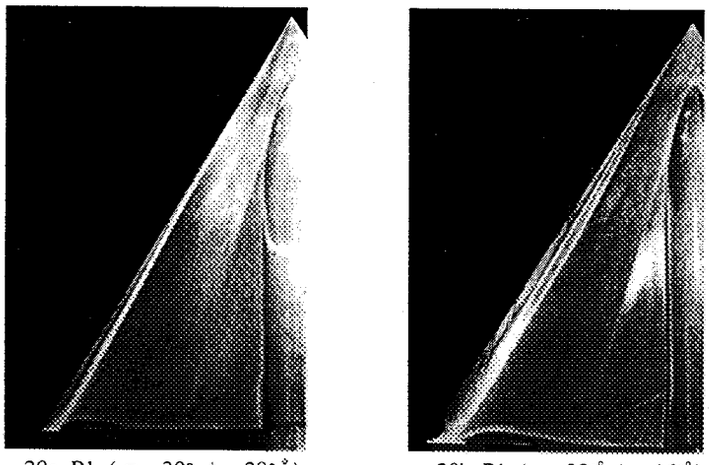

20a $P1_1$ (σ = 30°, ϕ = 28°) 20b $P1_2$ (σ = 30°, ϕ = 16°)

Fig. 20 Concentrated vortex pattern

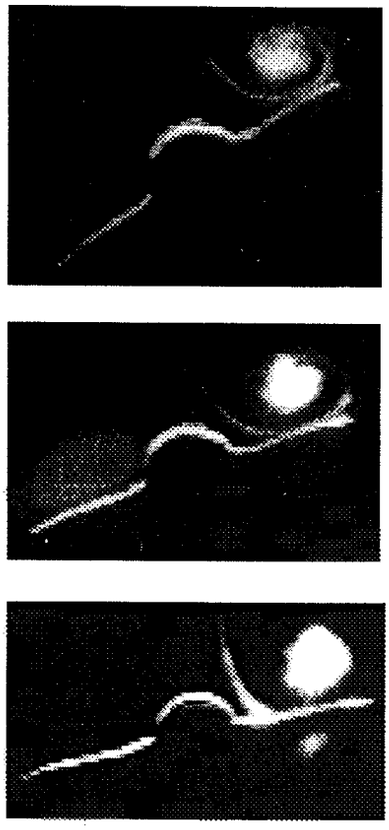

Fig. 21 Cross-section view of vortex
(σ=30°)

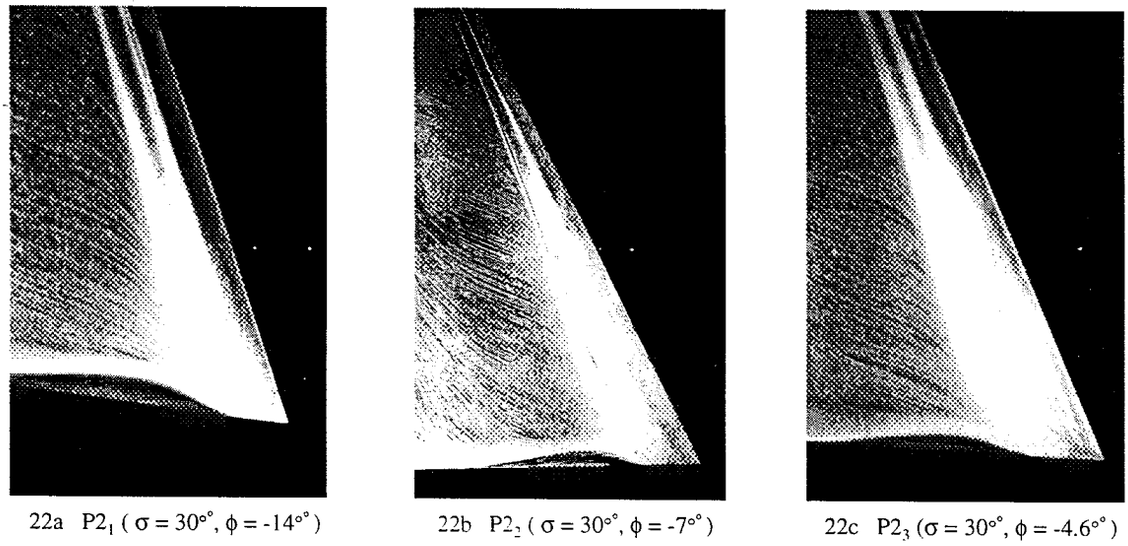

22a $P2_1$ (σ = 30°, ϕ = -14°) 22b $P2_2$ (σ = 30°, ϕ = -7°) 22c $P2_3$ (σ = 30°, ϕ = -4.6°)

Fig. 22 Vortex "whorl" patterns

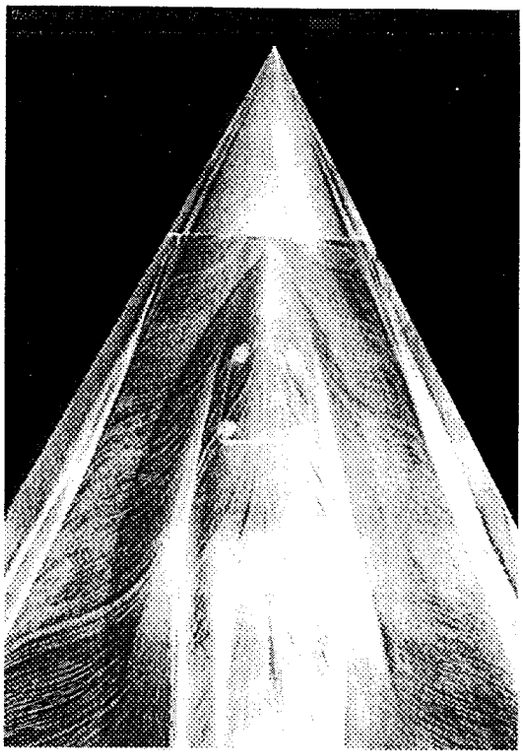

23a forward part $P3_1$:$P3_1$ ($\sigma = 30°$, $\phi = 0°$)

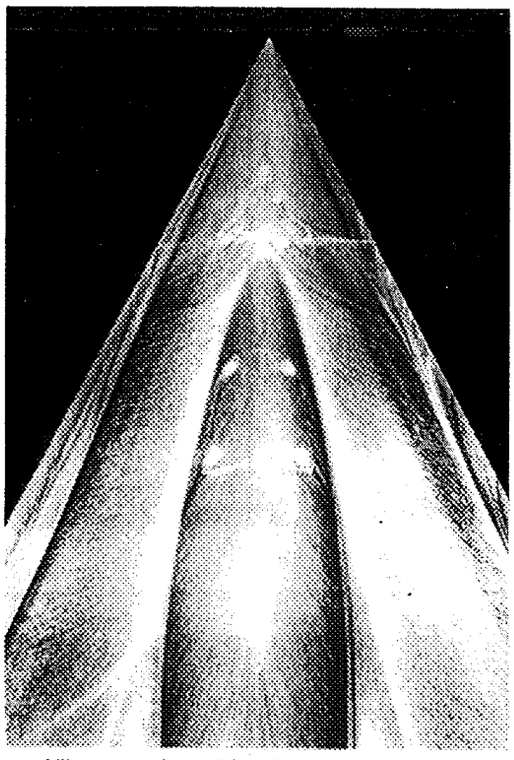

23b forward part $P3_1$:$P3_2$ ($\sigma = 35°$, $\phi = 2.5°$)

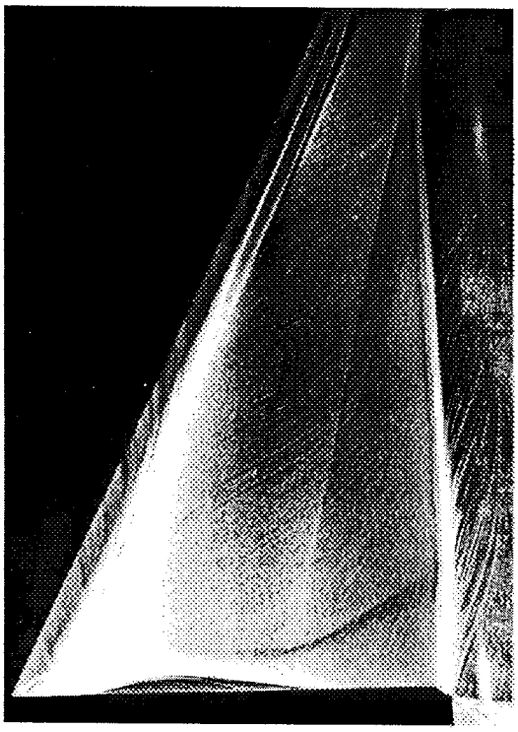

23c aft part of left wing $P3_1$ ($\sigma = 35°$, $\phi = 2.5°$)

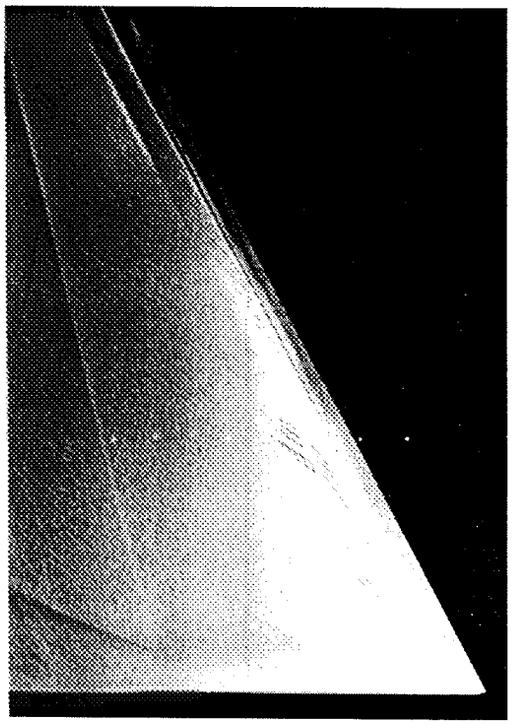

23d aft part of right wing $P3_2$ ($\sigma = 35°$, $\phi = 2.5°$)

Fig. 23 Vortex bursting patterns on different wing areas

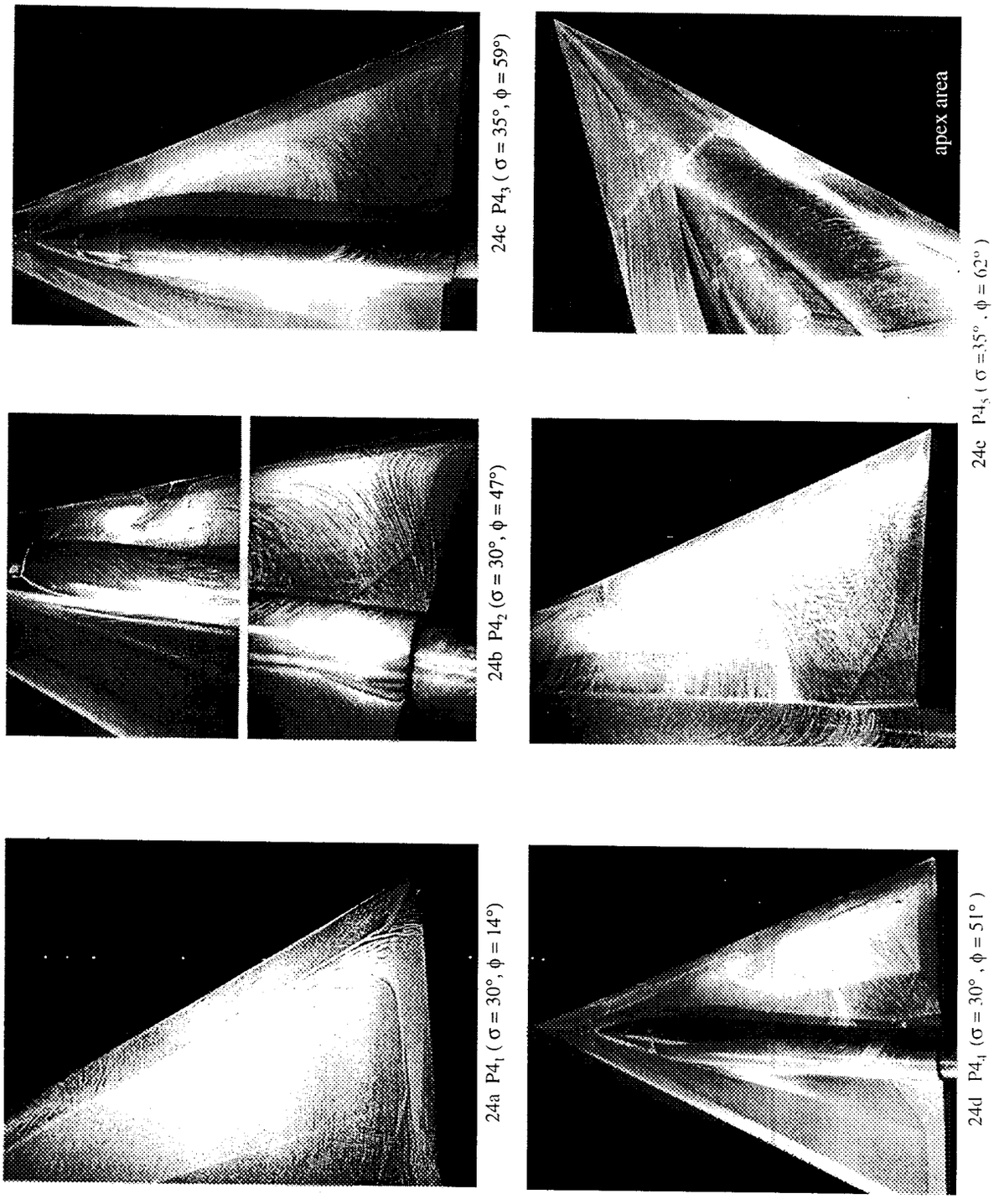

24a $P4_1$ ($\sigma = 30°$, $\phi = 14°$)
24b $P4_2$ ($\sigma = 30°$, $\phi = 47°$)
24c $P4_3$ ($\sigma = 35°$, $\phi = 59°$)
24d $P4_4$ ($\sigma = 30°$, $\phi = 51°$)
24c $P4_5$ ($\sigma = 35°$, $\phi = 62°$)

Fig. 24 Flow visualization of reverse patterns

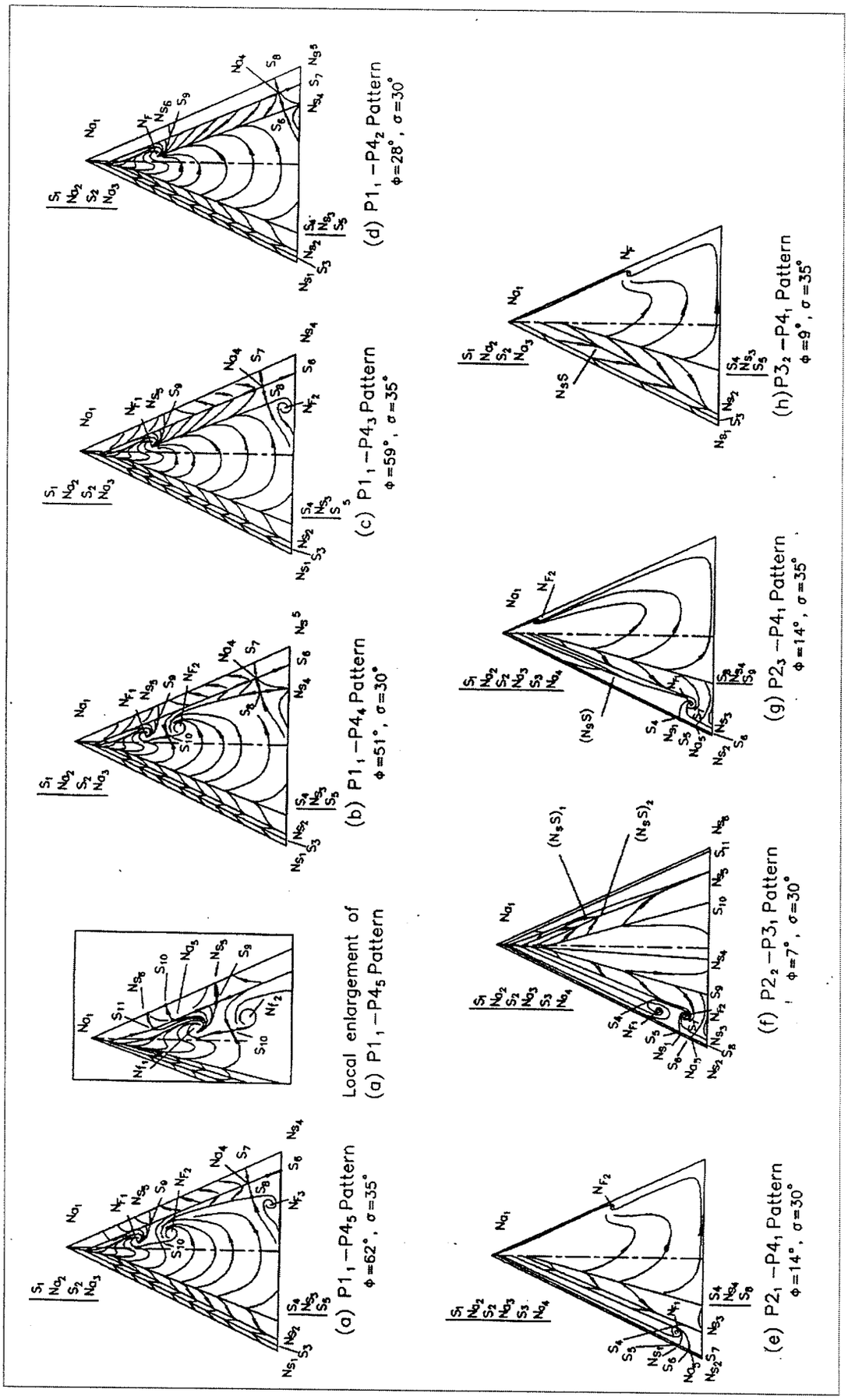

Fig. 25 Evolution of skin-friction topologies on 65° delta wing

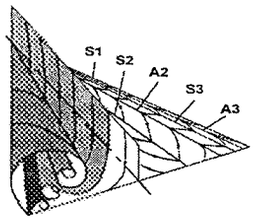

26a outboard tertiary vortex

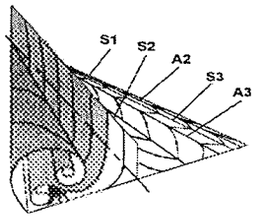

26b inboard tertiary vortex

Fig. 26 Different interpretations of secondary and tertiary vortices

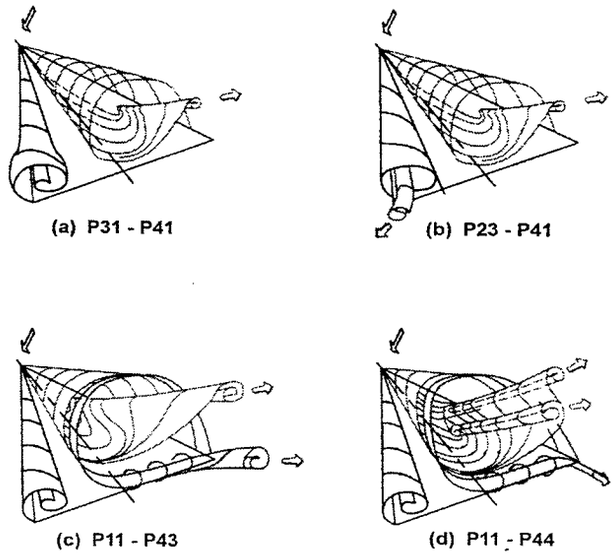

Fig. 27 Interpretations of surface flow topologies

Table 1 Comparisons between surface flow topology changes and measured critical states

Flow topologies (σ=30°)			Critical states	Flow topologies (σ=35°)			Critical states
ϕ°	Port	Starboard	ϕ°,σ°	ϕ°	Port	Starboard	ϕ°,σ°
0	$P3_1$	$P3_1$		0	$P3_1$	$P3_1$	
4	$P3_1$	$P3_1$		1.2	$P3_1$	$P3_1$	← ϕ=1.2°,σ=35°
4.6	$P2_2$	$P3_1$	← ϕ=5°,σ=29°	2.5	$P3_1$	$P3_2$	← ϕ=3.5°,σ=35°
4.8	$P2_2$	$P3_1$		6	$P3_1$	$P4_1$	
5.2	$P2_2$	$P3_1$		7	$P3_1/P2_3$	$P4_1$	
6	$P2_2$	$P3_1$		9	$P3_1/P2_3$	$P4_1$	
6.5	$P2_2$	$P3_1$		12	$P1_1/P2_3$	$P4_1$?	
7	$P2_2$	$P3_1$		14	$P1_1/P2_3$	$P4_1$?	
7.5	$P2_2$	$P4_1$(weak)	← ϕ=8.2°,σ=29° (?)	21	$P1_1$	$P4_1/P4_2$	
8.4	$P2_2$	$P4_1$		28	$P1_1$	$P4_2$	
10	$P2_2$	$P4_1$		37	$P1_1$	$P4_2$	
11.2	$P2_2$	$P4_1$	← ϕ=11.6°,σ=29°	42	$P1_1$	$P4_2$	
12	$P2_2 \leftrightarrow P2_1$	$P4_1$		59	$P1_1$	$P4_3$	← ϕ=62.1°,σ=35°
14	$P2_1$	$P4_1$		62	$P1_1$	$P4_5$	
16	$P2_1$	$P4_1$		67	$P1_1$	P5	
21	$P1_1$	$P4_2$		69	$P1_1$	P5	
28	$P1_1$	$P4_2$					
32	$P1_1$	$P4_2$					
40	$P1_1$	$P4_2$					
42	$P1_1$	$P4_2$					
47	$P1_1$	$P4_2$	← ϕ=50.1°,σ=29°				
51	$P1_1$	$P4_4$	← ϕ=51.5°,σ=29°				
57	$P1_1$	$P1_1$					